# VHCF response of as-built SLM AlSi10Mg specimens with large loaded volume

**Authors:**

A. Tridello[a], C.A. Biffi[b], J. Fiocchi[c], P. Bassani[d], G. Chiandussi[e], M. Rossetto[f], A. Tuissi[g], D.S. Paolino[h]


[a] Department of Mechanical and Aerospace Engineering, Politecnico di Torino, 10129 Turin, Italy, andrea.tridello@polito.it

[b] CNR ICMATE – Institute of Condensed Matter Chemistry and Technologies for Energy, 23900 Lecco, Italy, carloalberto.biffi@cnr.it

[c] CNR ICMATE – Institute of Condensed Matter Chemistry and Technologies for Energy, 23900 Lecco, Italy, jacopo.fiocchi@icmate.cnr.it

[d] CNR ICMATE – Institute of Condensed Matter Chemistry and Technologies for Energy, 23900 Lecco, Italy, paola.bassani@cnr.it

[e] Department of Mechanical and Aerospace Engineering, Politecnico di Torino, 10129 Turin, Italy, giorgio.chiandussi@polito.it

[f] Department of Mechanical and Aerospace Engineering, Politecnico di Torino, 10129 Turin, Italy, massimo.rossetto@polito.it

[g] CNR ICMATE – Institute of Condensed Matter Chemistry and Technologies for Energy, 23900 Lecco, Italy, ausonio.tuissi@cnr.it

[h] Department of Mechanical and Aerospace Engineering, Politecnico di Torino, 10129 Turin, Italy, davide.paolino@polito.it


**Corresponding Author:**

A. Tridello

*E-mail address*: andrea.tridello@polito.it

*Full postal address*:

C.so Duca degli Abruzzi 24,

Department of Mechanical and Aerospace Engineering – Politecnico di Torino,

10129 – Turin,

ITALY

*Phone number*: +39.011.090.6913

*Fax number*: +39.011.090.6999

**Abstract:**

It is well-known in the literature that fatigue is particularly critical for Additive Manufacturing (AM) parts, since internal defects originating during the AM process represent a critical site for crack initiation. In the literature, the High-Cycle-Fatigue (HCF) response of AM parts has been extensively investigated; however, there are few results on the Very-High-Cycle-Fatigue (VHCF) behavior of AM parts, even if the number of machinery components that may sustain VHCF is rapidly increasing in the last years.

The present paper investigates the VHCF response of an AlSi10Mg alloy produced through Selective Laser Melting. Ultrasonic tests are carried out on Gaussian specimens with a large loaded volume and show that fatigue failures in VHCF originate from surface and sub-surface defects with the same mechanism of HCF failures. P-S-N curves and fatigue strength at $10^9$ cycles are finally estimated to show the effect of defect size on the VHCF strength.

**Acronyms and nomenclature**

AM: Additive Manufacturing

SLM: Selective Laser Melting

VHCF: Very High Cycle Fatigue

$YS$: yield stress.

$UTS$: ultimate tensile strength.

$ETF$: elongation to failure.

$E_d$: Dynamic Young's Modulus

IET: Impulse Excitation Technique

HV: Vickers hardness

$s_{spec}$: stress amplitude measured by the gage bonded at the center of the Gaussian specimen (Gage B)

$s_{horn}$: stress amplitude measured by the gage bonded to the horn  (Gage A)

$s_{local}$: local stress amplitude, stress amplitude at the defect location.

P-S-N: Probabilistic-S-N curve

$r_{max}$: radius of the cross-section at the defect location

SIF: Stress Intensity Factor

$F_{\sqrt{a_{d,0}}}$: distribution of defect size

$\sqrt{a_{d,0}}$: square root of the projected area of the defect originating failure

LEVD: Largest Extreme Value distribution

$K_{th}$: SIF threshold

rv: random variable (rv)

$\mu$, $\sigma_Y$: mean and standard deviation of the fatigue life rv.

$c_Y$, $m_Y$, $n_Y$: constant coefficients

$N_f$: the number of cycles to failure

$Z$: standardized Normal rv.

$n_{ref}$: reference number of cycles.

$S_{corr}$: VHCF strength at the reference number of cycles.

$F_{S_{corr}}$: cumulative distribution function of the $S_{corr}$ rv.

$\mu_{S_{corr}}$, $\sigma_{S_{corr}}$: mean and standard deviation of the $S_{corr}$ rv.

# 1. INTRODUCTION

In the last decades, the use of Additive Manufacturing (AM) techniques for the production of metallic components has rapidly increased. AM permits to manufacture parts and components characterized by interesting mechanical properties and complex shapes, which could be hardly obtained by conventional manufacturing processes. Among the AM techniques for metals, Selective Laser Melting (SLM) is one of the most used and widely employed for the production of aluminum based parts, in particular of AlSi10Mg alloy components[1]. Technological aspects[2-4], static and fatigue mechanical properties[5-7] as well as thermal treatment procedures[8] of AlSi10Mg parts produced by SLM have been extensively investigated in the literature and AlSi10Mg components are currently adopted for many industrial applications.

The SLM process permits to manufacture parts characterized by promising quasi-static mechanical properties[9] but fatigue strength can be critical for SLM parts[10]. During the SLM building process, many defects originate within AM parts, such as porosities induced by vaporization of light elements, sintered powders and residual oxide layers. These AM defects are extremely dangerous for components subject to fatigue since they represent a critical initiation site for the fatigue crack and could lead to unexpected failures in the High Cycle Fatigue (HCF) and in the Very High Cycle (VHCF) regimes. In the literature, the HCF response of SLM parts has been extensively investigated[10]. However, there are still very few results on the VHCF behavior of SLM parts[11, 12], even if the number of machinery components that may sustain VHCF is rapidly increasing in the last years (see, e.g., the numerous applications where high frequency vibrations are present[13-19]. For these reasons, the experimental assessment of the VHCF response of AM parts is currently of utmost interest between researchers and industries working in the AM field and would permit a proper and safe design of AM components subject to fatigue loads for very high number of cycles.

The present paper deals with the VHCF response of an AlSi10Mg alloy produced through SLM. Fully reversed tension-compression tests were carried out by using the ultrasonic testing machine developed at the Politecnico di Torino[20-23]. Ultrasonic tests were performed on Gaussian specimens[22,24] with a large loaded volume (risk-volume). Tests on large risk-volumes permitted an accurate estimation of the defect size distribution[22, 24-26] and a reliable assessment of the VHCF response[22-26]. Fracture surfaces were observed with the Scanning Electron Microscope (SEM) and showed that fatigue failures in the VHCF region originated from surface and sub-surface defects, with the same mechanisms found in the literature for HCF failures[10]. P-S-N curves and fatigue strength at $10^9$ cycles were finally estimated to show the effect of defect size on the VHCF strength.

# 2. MATERIAL AND METHODS

The present Section describes the experimental activity in detail: subsection 2.1 concerns the material properties and the SLM process parameters; subsection 2.2 reports the base mechanical properties of the investigated material; subsection 2.3 describes the ultrasonic testing machine used for the VHCF tests.

## 2.1. Material and SLM process parameters

Spherical gas atomized AlSi10Mg powders, whose nominal chemical composition is reported in Table 1, were used for the experimental tests. The particles size can be approximately featured with a Gaussian distribution in the range 20−63 μm, with average size of approximately 45 μm.

Table 1: Chemical composition of the AlSi10Mg powder (wt. %)

| Si | Mg | Cu | Ni | Fe | Mn | Ti | Al |
|----|-----|--------|--------|--------|-------|--------|------|
| **10** | 0.4 | < 0.25 | < 0.05 | < 0.25 | < 0.1 | < 0.15 | bal. |

A SLM Solutions (model 500 HL quad 4 × 400 W) Selective Laser Melting system, equipped with 4 continuous wave fiber lasers having maximum power of 400W, was used to manufacture the samples for the experimental tests. All the samples were built in the x-y plane[27] and tested in the as built condition. Standard process parameters (Table 2) provided by the SLM producer were used for the production of the specimens.

Table 2: SLM process parameters used for building the AlSi10Mg specimens.

| *Power* | *Building plate temperature* | *Scanning speed* | *Spot size* | *Hatch distance* | *Layer thickness* | *Atmosphere* |
|---------|------------------------------|------------------|-------------|------------------|-------------------|--------------|
| 350 W | 150 °C | 1.15 m/s | 80 µm | 170 µm | 50 µm | Argon |

The microstructure of the AlSi10Mg specimens used for the experimental tests was deeply investigated in Ref.[8, 28]: the manufactured specimens showed the typical as-built AM microstructure, characterized by a columnar solidification structure that follows the shape of the localized melting pools originated by the building process.

## 2.2. SLM AlSi10Mg base mechanical properties

The base mechanical properties (tensile strength, Dynamic Young modulus and Vickers hardness) of the SLM AlSi10Mg used for the ultrasonic VHCF tests were evaluated according to different experimental procedures.

Tensile tests were carried out on standard dog bone specimens by using a MTS 2/M machine (strain rate of $0.015 \text{ min}^{-1}$), equipped with extensometer. The resulting mechanical properties (Elastic modulus, $E$, yield stress, $YS$, ultimate tensile strength, $UTS$, and elongation to failure, $ETF$) are reported in Table 3.

Table 3: Static mechanical properties of as built samples.

| $E$ [GPa] | $YS$ [MPa] | $UTS$ [MPa] | $ETF$ [%] |
|-----------|------------|-------------|-----------|
| **70. 1 ($\pm$ 0. 6)** | 287.4 ($\pm$ 5) | 413.2 ($\pm$ 7) | 5.5 ($\pm$ 0.1) |

The Dynamic Young's Modulus, $E_d$, was assessed through the Impulse Excitation Technique (IET). Five rectangular bars were produced through SLM with the same process parameters reported in subsection 2.1. The first longitudinal resonance mode of vibration was used for the computation of the Dynamic Young's Modulus, according to Ref.[29]. The average Dynamic Young's Modulus was equal to 71.9 GPa, with a limited standard deviation of 0.6 GPa.

Vickers hardness was finally measured on four samples obtained from the specimens failed during the VHCF tests (Section 2.4). Hardness tests were performed according to Ref.[30]. Fig. 1 shows the Vickers hardness variation within the specimen cross-section. According to the reference system reported in the Figure,

Vickers hardness was measured at the center of the cross-section and at two different locations (radius and half of the radius) along the positive and the negative x and y directions.
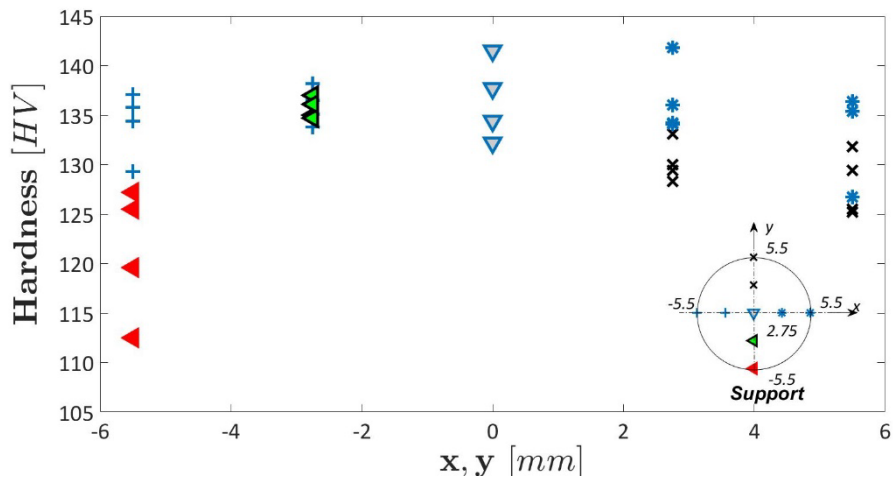


Figure 1: Distribution of the Vickers hardness within the specimen cross-section.

According to Fig. 1, the Vickers hardness is almost constant within the cross-section, except for the region close to the support structures used for the AM production and removed at the end of the SLM process. The average hardness within the cross-section is equal to 134 HV, whereas it slightly reduces near the support region (mean value equal to 121 HV). However, the scatter is limited and the maximum variation (11%) is comparable to the variation reported in the literature[25].

## 2.3. Ultrasonic testing configuration

Ultrasonic VHCF tests were carried out on Gaussian specimens[22-24] with a risk-volume of 2300 mm$^3$ (volume of material subjected to a stress amplitude larger than 90% of the maximum stress amplitude, according to Re.[25-26]). Gaussian specimens were recently proposed by the research group of the Politecnico di Torino to increase the tested risk-volume in ultrasonic fatigue tests, with respect to that attainable with traditional hourglass and dog-bone specimens[31]. According to the well-known dependency between defect size and risk-volume (size-effect), tests on large risk-volumes allow for a more proper assessment of the defect size distribution and a reliable estimation of the VHCF response. Gaussian specimens were tested in the as-built condition, which represents the worst condition with respect to fatigue loads. Therefore, tests on as-built specimens permit to assess a lower and conservative limit for the VHCF response. Fig. 2 shows the geometry of the Gaussian specimen used for the experimental tests.
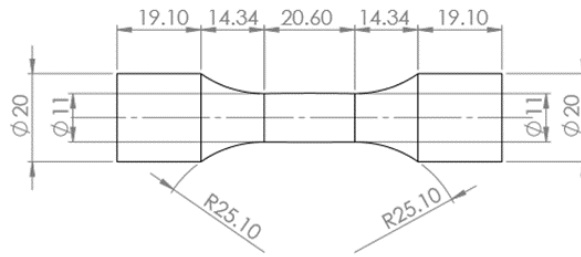
Figure 2: Geometry of the Gaussian specimen used for the experimental tests.

Before the experimental tests, specimens were finely polished by using sandpapers with increasing grit (from 240# to 1200#) in order to remove macroscopic surface defects and residual parts of the support structures. The surface roughness Ra of the tested specimens, equal to $1.41 \pm 0,26$ μm, was measured on five specimens by using a Mitutoyo Surftest SV-500 instrument.. Fig. 3 shows a Gaussian specimen before (Fig. 3 (a)) and after the polishing process (Fig. 3 (b)).
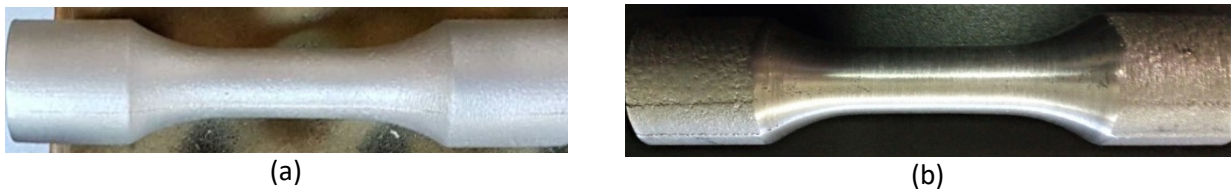


(a)

(b)

Figure 3: Gaussian specimen used for the ultrasonic VHCF tests: (a) specimen before the polishing process; specimen after the polishing process.

Fully reversed tension-compression tests at constant stress amplitude were carried out up to failure or up to $10^9$ cycles (runout specimens) by using two Ultrasonic Fatigue Testing Machines (UFTMs) developed at the Politecnico di Torino. The UFTMs consist of: (a) an ultrasonic generator (Branson DCX 4 kW) that generates an electric sinusoidal signal with frequency of 20 kHz; (b) a piezoelectric transducer that converts the electric signal in mechanical vibration; (c) two mechanical amplifiers (a booster and a horn), rigidly connected to the piezoelectric transducer, that amplify the vibration amplitude; (d) the specimen, rigidly connected to the horn, that is subjected to fully reversed tension-compression load. During the tests, specimen temperature within the risk-volume was monitored by using an infrared sensor and three vortex tubes were used for cooling the specimen. Ultrasonic fatigue tests were run continuously and specimen temperature kept constant at about 25° C. The stress amplitude within the specimen risk-volume was kept constant through a closed loop control based on the strain measured by a strain gage (HBM 1-XY31-1.5/350) attached to the horn (Gage A). The correlation between the stress amplitude within the risk-volume and the strain measured by Gage A was verified by bonding a second strain gage (Gage B) at the center of the Gaussian specimen.

Fig. 4 shows the stress amplitude measured by Gage B, $s_{spec}$, with respect to the stress amplitude measured by Gage A, $s_{horn}$. The two stresses, $s_{spec}$ and $s_{horn}$, were obtained from the measured strain amplitude and by considering the average Dynamic Young modulus (Section 2.2). The calibration procedure was performed on three specimens at four increasing voltage amplitudes imposed by the piezoelectric transducer.
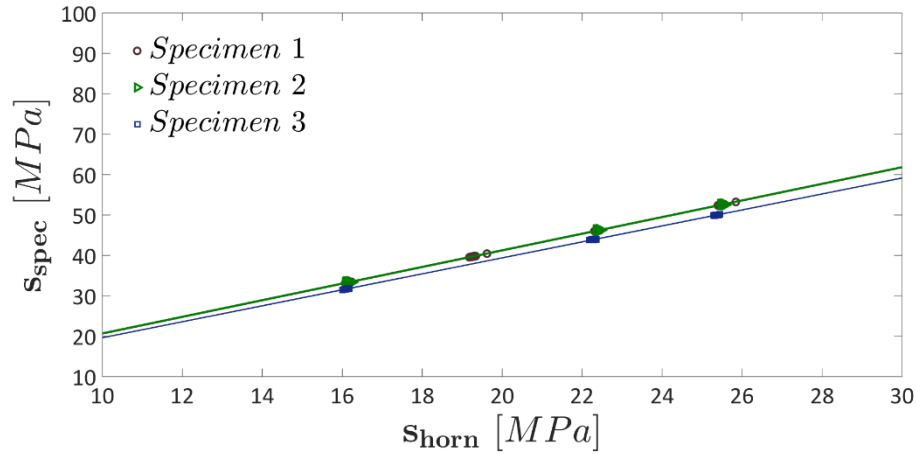
Figure 4: Stress amplitude measured by Gage B, $s_{spec}$, with respect to the stress amplitude measured by Gage A, $s_{horn}$.

According to Fig. 4, the difference between the stress amplitude measured at the specimen center in the three tested specimens is smaller than 1 MPa, confirming that Gaussian specimens produced through AM can be tested and that the stress amplitude variation among the specimens is limited notwithstanding the large manufacturing tolerances typical of AM processes.

Specimen temperature on the external surface of the risk-volume was also continuously monitored during the tests with an infrared temperature sensor (OPTRIS CT-LT-15) and kept below 298 K by using three vortex tubes placed near the specimen center. The temperature uniformity within the risk-volume was also verified, according to Ref.[32, 33].

## 3. EXPERIMENTAL RESULTS

The present Section describes the experimental results: subsection 3.1 reports the experimental dataset and subsection 3.2 concerns the fractographic analyses.

## 3.1. Experimental dataset

Ultrasonic tests were carried out at nominal stress amplitudes (i.e., at the center of the specimen) between 60 MPa and 95 MPa. 9 out of 17 specimens failed in the range between $6.85 \cdot 10^4$ and $9.79 \cdot 10^9$, whereas 6 out 17 specimens did not fail at $10^9$ cycles (runout specimens). Two specimens failed before $10^4$ cycles due to a large surface scratch in the area where support structures were removed and are not considered in the following analysis since the applied stress amplitude was not properly controlled.

Fracture surfaces were observed with an optical microscope and a Scanning Electron Microscope, SEM (FE-SEM SU70, Hitachi) to investigate the failure origin. All the fatigue failures originated from surface or subsurface defects. For the analysis of the experimental data, the stress amplitude at the defect location, local stress amplitude $s_{local}$, was used. $s_{local}$ was assessed through Finite Element Analysis (FEA) by considering the exact location of each defect (or group of defects). Defect locations along the axial and the radial direction were measured with a digital caliper (resolution of 0.01 mm) and through digital image processing of the fracture surface, respectively. Fig. 5 shows the S-N plot of the experimental data.
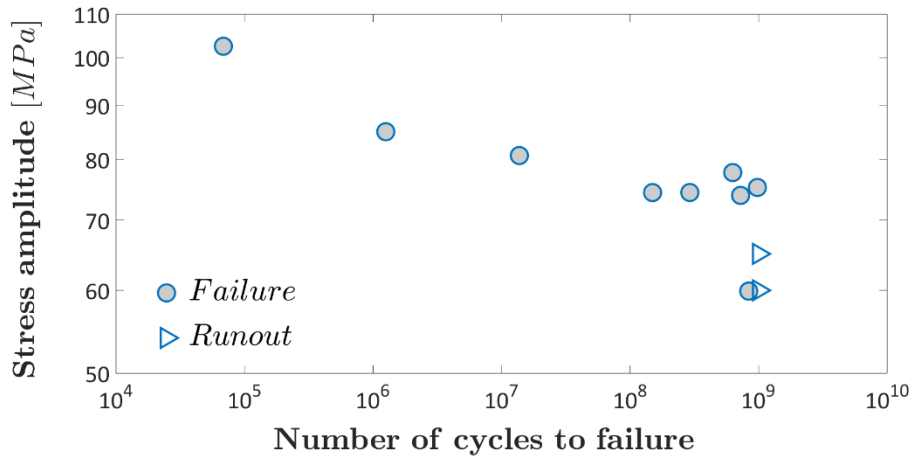
Figure 5: S-N plot of the experimental data.

As shown in Fig. 5, for stress amplitudes below 80 MPa failures occurred in the VHCF region, whereas for stress amplitudes larger than 85 MPa failures occurred before $10^7$ cycles, in the HCF region. Experimental failures in the VHCF region show a large scatter, mainly due to the large variability of the defect size. Due to this, Probabilistic-S-N (P-S-N) models for the description of the S-N data must not neglect the statistical distribution of the defect size.

### 3.2. Defect analysis

The defects at the origin of the fatigue failure are analyzed in detail in this subsection. Fig. 6 shows the distribution of defects originating failure within the specimen cross-section. According to the reference system reported in Fig. 6, the location of the defects along the $x$ and the $y$ directions is normalized with respect to the radius of the cross-section ($r_{max}$).
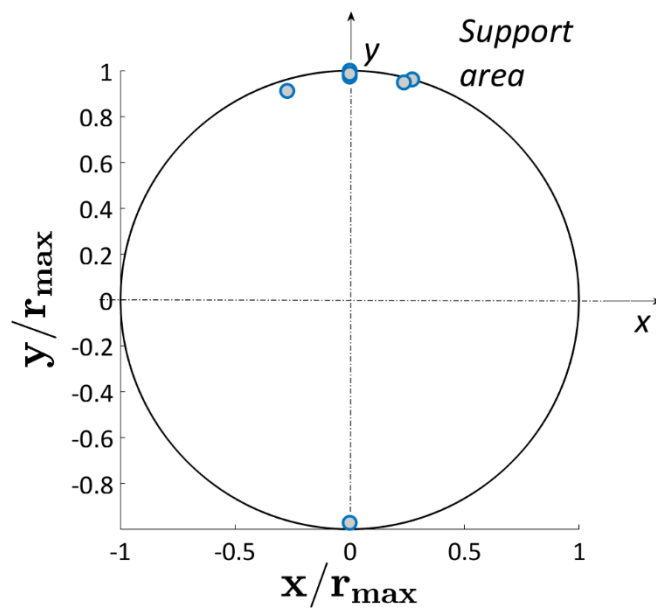


Figure 6: Distribution of defects originating failures within the specimen cross-section.

According to Fig. 6, all the fatigue failures originated from a surface defect or from a subsurface defect (maximum distance from the free surface equal to 275 μm), in agreement with the results reported in Ref.[10].

9

The region close to the surface shows a large concentration of defects; therefore, the removal of a thin layer of material during the polishing process did not permit to eliminate all the critical surface defects. Surface defects are more critical than internal defects: according to Ref.[25], the Stress Intensity Factor (SIF) associated to a surface defect is about 32% larger than the SIF associated to an internal defect with the same size. Therefore, even if larger internal defects are present, they are not critical for the VHCF life, in agreement with Ref.[10] Moreover, as-built specimens are characterized by high residual stresses, which originate due to the high temperature gradient during the AM process. Distribution of residual stresses is not uniform within the manufactured part and, according to Ref.[34], they are generally higher in the region close to the surface. The interaction between defects and local residual stresses can be critical and can contribute to the crack nucleation process, further justifying the high concentration of fatigue failures originating near the surface.

Fig. 7 shows an example of fracture surface characterized by a large concentration of defects close to the surface and by one large non-critical internal defect.
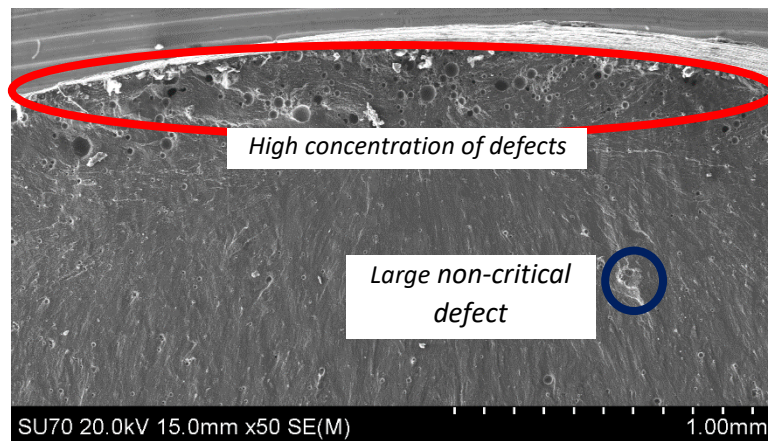


Figure 7: Example of a fracture surface showing a large concentration of defects close to the surface and one non-critical internal defect.

The morphology of defects originating failure was also analyzed. Three types of defects were found with SEM analyses (Fig. 8): single surface defect, Fig. 8 a); single sub-surface defect, Fig. 8 b); clusters of pores, Fig. 8 c).
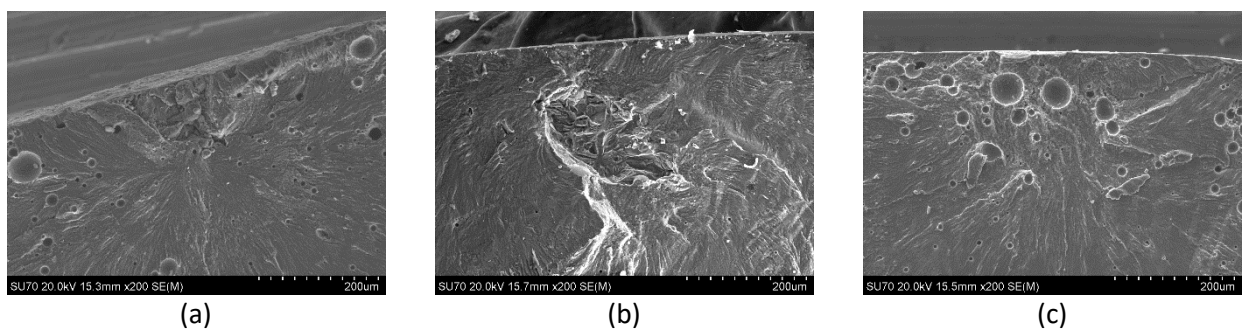


Figure 8: Types of defects originating failure: (a) single surface defect; (b) single sub-surface defect; (c) clusters of pores.

Fig. 8 a) shows a typical surface defect (2 out of 9 failures) in the support region, probably originated during the removal of the supports. The mechanical removal of the support structures is particularly critical in AM parts and large critical defects can originate during this process. Tests on large risk-volumes and on *as-built* specimens permit to estimate the effect of this type of defects, which are less frequent but are particularly detrimental for the VHCF life.

Fig. 8 b) shows a sub-surface defect with an irregular shape. Only in one case the fatigue failure originated from this type of defect. Energy Dispersive X-ray spectroscopy (EDX) technique showed that it is not an oxide-type defect, but it probably originated due to an incomplete fusion of the powder during the building process.

Fig. 8 c) shows a cluster of pores. Pores were at the origin of the fatigue failure in almost all the cases (6 out of 9): indeed, even if pores have smaller size compared to other defects, cluster of pores may become critical due to the interaction between single pores, according to Ref.[25].

The distribution of the defect size, $F_{\sqrt{a_{d,0}}}$, was finally analysed: according to Ref.[25], $\sqrt{a_{d,0}}$ is the square root of the projected area of the defect originating failure and is assumed to follow a Largest Extreme Value Distribution (LEVD). Defects which led to VHCF failure, and, in general, defects originating during the AM process are characterized by an irregular morphology and shape. Defect morphology could affect the VHCF response. However, even for AM parts, the fatigue response is mainly affected by the defect size, rather than by its shape and chemical composition. In case of defects with irregular morphology and shape, an equivalent defect size should be considered to estimate the distribution of defect size[25]. In the following, the equivalent defect size was estimated according to Ref.[25, 35]. Fig. 9 shows the Gumbel Plot of the experimental data, together with the estimated model.



$$\mathbf{F}_{\sqrt{\mathbf{A}_{d,0}}} = \mathbf{e}^{-\mathbf{e}^{-\frac{\sqrt{\mathbf{a}_{d,0}}-142.4}{30.4}}}$$
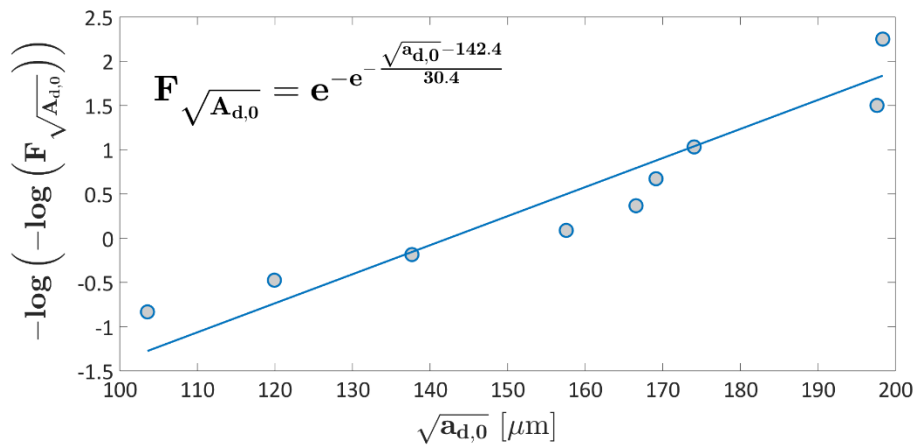
Figure 9: Gumbel plot of the experimental data and estimated LEV distribution.

According to Fig. 9, $\sqrt{a_{d,0}}$ values are in the range $[103 - 198]$ μm, which is close to the range found in the literature[10] for the same material produced through SLM.

The analyses performed in this subsection confirm the need for testing large and statistically relevant risk-volumes for an accurate assessment of the defect size distribution in AM parts and, accordingly, their VHCF response. Indeed, as highlighted by the experimental results, different types of defects were at the origin of the fatigue failure in the investigated SLM AlSi10Mg alloy. A cluster of pores was the most common defect (67% of the investigated failure), in agreement with literature data, whereas irregular defects due to

incomplete fusion and surface defects were found in one case (11%) and in two cases (22%), respectively. Moreover, experimental results suggest that metallographic inspections on polished samples[26] may not provide an accurate estimation of the defect size distribution and of the VHCF response for AM parts, since rare and critical defects (e.g., surface defects originating during the removal of support structures or irregular defects) are very unlikely in small areas.

The distribution of the equivalent defect size, estimated according to the methodology proposed by Murakami[25-35], is used for the estimation of the P-S-N curves and of the fatigue strength at $10^9$ cycles, according to a statistical model recently proposed by the research group of the Politecnico di Torino[36,37].

## 4. P-S-N CURVES

The present Section analyzes the effect of the defect size on the VHCF life: subsection 4.1 concerns the identification of the threshold for crack propagation from the experimental data; whereas subsection 4.2 deals with the estimation of the P-S-N curves and of the fatigue strength at $10^9$ cycles, according to the model proposed in Ref.[36,37].

### 4.1. Stress Intensity Factor Threshold

The SIF threshold, $K_{th}$, was estimated by considering the defect size or the equivalent defect size measured on fracture surface. A linear model in a log-log plot is considered for $K_{th}$, according to Ref.[10, 37]. Fig. 10 shows the $K_{th}$ values with respect to $\sqrt{a_{d,0}}$ in a log-log scale, together with the estimated linear model. The median, the 0.1-th and the 0.9-th quantiles of the $K_{th}$ function are also depicted in Fig. 10.
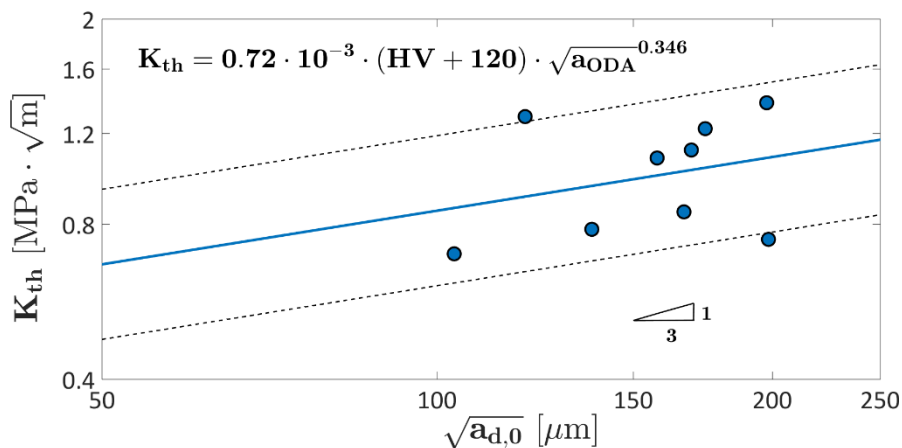


Figure 10: SIF threshold, $K_{th}$, with respect to the defect size $\sqrt{a_{d,0}}$.

According to Fig. 10, the linear model is in agreement with the experimental data[10]. The slope of the interpolating function, equal to 0.346 (in the log-log scale) is close to the values reported in Ref.[10] (1/2 for defects smaller than 800 μm and 1/3 for a defect range of $[200 - 800]$ μm).

## 4.2. P-S-N curves

P-S-N curves were finally estimated by taking into account the defect size and its statistical distribution. In the present paper, the model proposed in Ref.[36-37] was used for the estimation of the P-S-N curves. The experimental data do not show a clear asymptotic behavior at $10^9$ cycles: at the lowest applied stress amplitude of 57 MPa, 3 runouts at $10^9$ cycles and a fatigue failure close to the runout number of cycles ($8.36 \cdot 10^8$) were found, suggesting that further experimental tests at a larger number of cycles should be performed to verify the presence of a VHCF limit. Therefore, according to the model in Ref.[34] and in Ref.[35] ("One failure mode due to one cause without fatigue limit"), the logarithm of the fatigue life is a Normal random variable (rv) with constant standard deviation, $\sigma_Y$, and mean, $\mu$, that linearly depends on the logarithm of the stress amplitude and of the defect size:

$$\mu = c_Y + m_Y \log[s_{local}] + n_Y \log_{10}\left[\sqrt{a_{d,0}}\right], \tag{1}$$

being $c_Y$, $m_Y$ and $n_Y$ constant coefficients. From this model, P-S-N curves as a function of the defects size (conditional P-S-N curves) can be estimated.

Fig. 11 shows the conditional P-S-N curves estimated from the experimental data (grey circles). Fig. 11 a) shows the conditional P-S-N curves (0.5-th, the 0.1-th and the 0.9-th quantile) for the defect with median size ($\sqrt{a_{d,0}} = 166$ µm), together with the experimental corresponding failure (blue circle). Fig. 11 b) shows the median conditional P-S-N curves for values of the initial defect size equal to 103 µm (smallest defect found experimentally) and 198 µm (largest defect found experimentally). In Fig. 11 b), the blue circle and the red circle represent the experimental failure for $\sqrt{a_{d,0}} = 103$ µm and for $\sqrt{a_{d,0}} = 198$ µm, respectively.
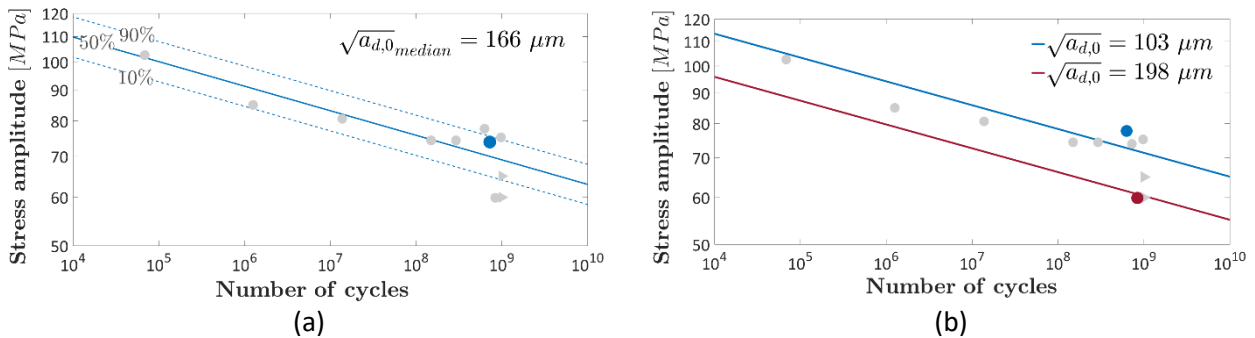


Figure 11: Conditional P-S-N curves: a) 0.5-th, 0.1-th and 0.9-th quantiles of the conditional P-S-N curves for a defect with median size ($\sqrt{a_{d,0}} = 166$ µm); b) median P-S-N curves for different $\sqrt{a_{d,0}}$ values.

According to Fig. 11 a), the proposed model is in agreement with the experimental data: the experimental failure originating from the defect with the median size is included within the estimated 80% confidence interval. Regarding Fig. 11 b), the median P-S-N curves move downward with the defect size: for a fatigue life of $10^9$ cycles, a 15% reduction of the VHCF strength is found passing from $\sqrt{a_{d,0}} = 103$ µm to $\sqrt{a_{d,0}} = 198$ µm. The proposed P-S-N curves can be employed to estimate the fatigue life if the largest defect size in the AM components is known, for example after a CT scan.

From the conditional model, the marginal P-S-N curves (P-S-N curves not conditioned to the initial defect size) can be estimated by considering the LEV distribution of the defect size, according to Ref.[37]. Fig. 12 shows

the median, the 0.01-th, 0.1-th and the 0.9-th quantiles of the P-S-N curves, together with the experimental data.
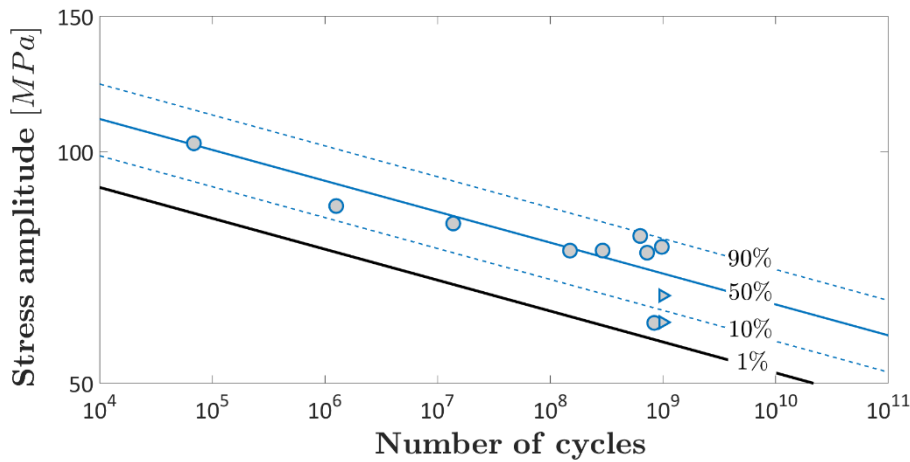


Figure 12: Marginal P-S-N curves (not conditioned to the inclusion size) estimated from the experimental data.

Fig. 12 shows that the estimated P-S-N curves are in good agreement with the experimental data: about 90% of the experimental failures are included with the 0.1-th and the 0.9-th P-S-N curves. Moreover, the 0.01-th P-S-N curve is below all the experimental failures and it proves to be a conservative solution as a design curve for AM parts[22].

The proposed P-S-N curves are estimated by considering the (surface and sub-surface) defects that led to VHCF failure. It must be pointed out that, according to Ref.[38], defect location affects the VHCF response. In order to take into account the influence of defect location, an equivalent defect size (Section 3.2) was estimated following the procedure reported in Ref.[25, 35]. By considering the equivalent defect size, the defect location and the interaction between defects was therefore taken into account

Moreover, literature results on tests on AlSi10Mg specimens can be considered for the sake of comparison. In Ref.[39, 40], rotating bending fatigue tests were carried out on as-built AlSi10Mg specimens with comparable roughness. In Ref.[39], the fatigue strength at $10^7$ cycles found experimentally is about 90 MPa (roughness 1.5 µm): the corresponding axial fatigue strength is 65 MPa (loading factor of 0.7) and about 35% smaller than the fatigue strength found in the present paper. The difference can be mainly due to the different process parameters considered in the AM manufacturing process and, accordingly, to the different inclusion size.

By taking into account Ref.[40], the fatigue strength at $10^7$ cycles (roughness 1.5 µm) is about 125 MPa, with a corresponding axial fatigue strength of about 90 MPa (loading factor of 0.7), which is very close to the fatigue strength found experimentally in the paper.

In Ref.[41], ultrasonic fully reversed tension-compression tests on specimens obtained through conventional process were carried out. The fatigue strength at $10^9$ cycles found in Ref.[41] is about 90 MPa, 30% larger than the fatigue strength at $10^9$ cycles found in the paper. The different size of superficial defects could justify the smaller fatigue strength of specimens obtained through the AM process. According to the experimental results, if the superficial layer of material, where a high concentration of defects is found, could be removed, the difference between the VHCF strength obtained by testing the SLM and the wrought AlSi10Mg (obtained through traditional processes) could be significantly reduced.

Another solution to model the effect of defect size on the VHCF strength is to gather all the experimental failures at a reference number of cycles to failure, $n_{ref}$. According to the procedure reported in Ref.[22, 42] the logarithm of the fatigue life can be expressed as:

$$\log_{10}[N_f] = c_Y + m_Y \log[s_{local}] + n_Y \log_{10}[\sqrt{a_{d,0}}] + Z\sigma_Y,$$ (2)

being $N_f$ the number of cycles to failure, $Z$ the standardized Normal rv; whereas the VHCF strength, $S_{corr}$, at $n_{ref}$ is given by:

$$\log_{10}[S_{corr}] = \left(-\frac{c_Y}{m_Y} + \frac{\log_{10}[n_{ref}]}{m_Y} - \frac{n_Y}{m_Y}\log_{10}[\sqrt{a_{d,0}}]\right) + Z\frac{\sigma_Y}{-m_Y}.$$ (3)

Through easy passages, it can be shown that $S_{corr}$ is a Normal rv with mean equal to $\mu_{S_{corr}}$ ($\mu_{S_{corr}} = -\frac{c_Y}{m_Y} + \frac{\log_{10}[n_{ref}]}{m_Y} - \frac{n_Y}{m_Y}\log_{10}[\sqrt{a_{d,0}}]$) and standard deviation $\sigma_{S_{corr}}$ equal to $-\frac{\sigma_Y}{m_Y}$:

$$F_{S_{corr}} = \Phi\left[\frac{s_{corr} - \mu_{S_{corr}}}{\sigma_{S_{corr}}}\right].$$ (4)

Therefore, by substituting $F_{S_{corr}}$ with $\alpha$ and solving Eq. 2 with respect to $s_{corr}$, the $\alpha$ quantile of the fatigue strength at $n_{ref}$ for an initial defect size equal to $\sqrt{a_{d,0}}$ can be estimated. Fig. 13 shows the probability density functions of $S_{corr}$ at $n_{ref} = 10^9$ for an initial defect size equal to 50 μm and to 198 μm.
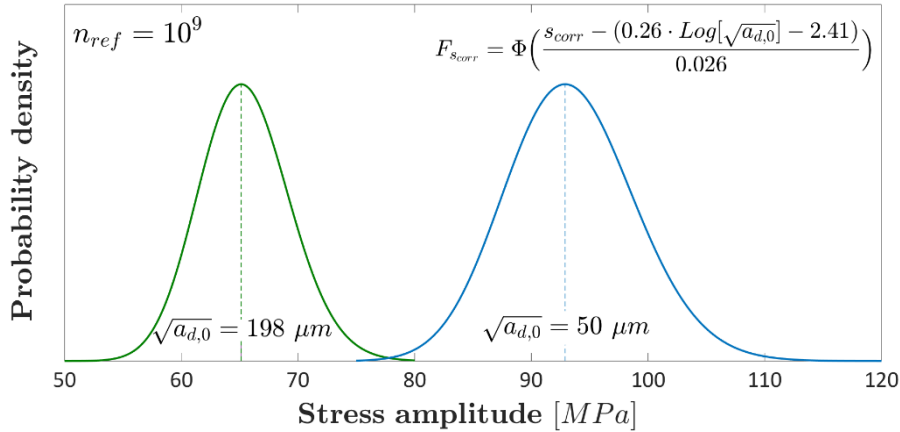


Figure 13: Probability density function of $S_{corr}$ at $n_{ref} = 10^9$.

According to Fig. 13, the mean fatigue strength significantly decreases with $\sqrt{a_{d,0}}$ (about 30% reduction). The proposed methodology of gathering all the experimental failures can also be effectively employed for evaluating and quantifying the influence of the defect size on the VHCF strength of AM parts.

## 5. CONCLUSIONS

In the paper, the Very-High-Cycle Fatigue (VHCF) response of an as-built AlSi10Mg alloy produced through Selective Laser Melting (SLM) was experimentally investigated. Ultrasonic fully reversed tension compression-compression tests were carried out on Gaussian specimens with a large risk-volume of $2300 \ mm^3$. Experimental results showed that failures in the VHCF region at small applied stress amplitudes could occur and originate from large defects with the same mechanism found in High-Cycle Fatigue (HCF) tests.

The defects originating failure were investigated in detail. Fatigue failures originated from surface and sub-surface defects (maximum distance from the surface of 275 μm) in all the investigated cases. Three types of critical defects were found: surface defects originated during the removal of the support structures, internal defects due to incomplete fusion and cluster of pores concentrated near the specimen surface. Clusters of pores were at the origin of the fatigue failures in most of cases (67%). The region close to the surface was found to be critical for the VHCF response and larger non-critical internal defects were found far from the external surface. The removal of a thin layer of material during the polishing process was not sufficient for avoiding surface failures; therefore, only the optimization of the SLM process parameters or the removal of a thicker layer of material (e.g., through machining) could eventually permit to enhance the VHCF response of AM parts.

Experimental results highlighted the need for testing large risk-volumes for a proper assessment of the VHCF response of AM parts. Tests on small volumes (those typical of hourglass specimens) would not permit a reliable assessment of the defect size distribution and, accordingly, of the VHCF response. Moreover, experimental results pointed out that metallographic inspections on polished samples may be misleading for the prediction of the VHCF response of AM parts: the correct prediction of large critical defects (e.g., surface defects originating during the removal of support structures or irregular defects) from small inspected areas requires a risky extrapolation that may also lead to a non-conservative estimation of the VHCF response.

Finally, Probabilistic-S-N (P-S-N) curves were estimated from the experimental data. Conditional P-S-N curves (P-S-N curves as a function of the defect size) and marginal P-S-N curves (not conditioned to the initial defect size) were found to be in agreement with the experimental data. The 0.01-quantile (99% reliability) of the marginal P-S-N curve was below all the experimental failures and, therefore, it can be conservatively employed when designing AM parts under VHCF.

To conclude, experimental results pointed out that the VHCF response of AM parts can be properly assessed only if the defect size distribution is accurately estimated. Indeed, statistical models for the estimation of the VHCF life must necessarily take into account the defect size distribution to ensure a safe design methodology and to prevent unexpected and dangerous failures in the VHCF region.

## REFERENCES

1 Olakanmi, E.O., Cochrane, R.F., Dalgarno, K.W. A review on selective laser sintering/melting (SLS/SLM) of aluminum alloy powders: processing, microstructure and properties. *Prog. Mater. Sci.* 2015; **74**: 401-477.

2 Aboulkhair, N.T., Everitt, N.M., Ashcroft, I., Tuck, C. Reducing porosity in AlSi10Mg parts processed by selective laser melting. *Additive Manufacturing*. 2014; **1**: 77–86.

3 Read, N., Wang, W., Essa, K., Attallah, V. Selective laser melting of AlSi10Mg alloy: Process optimisation and mechanical properties development. *Mater. Design*. 2015; **65**: 417–424.

4 Rao, H., Giet, S., Yang, V., Wu, V., Davies, C.H.J. The influence of processing parameters on aluminium alloy A357 manufactured by Selective Laser Melting. *Mater. Design*. 2016; **109**: 334–346.

5 Maskery, I., Aboulkhair, N.T., Tuck, C., Wildman, R.D., Ashcroft, I.A., Everitt, N.M., Hague, R.J.M. Fatigue performance enhancement of selectively laser melted aluminium alloy by heat treatment. *Solid Free. Fabr. Symp.* 2015: 1017–1025.

6 Siddique, S., Imran, M., Wycisk, E., Emmelmann, C., Walther, F. Influence of process-induced microstructure and imperfections on mechanical properties of AlSi12 processed by selective laser melting. *J. Mater. Process. Technol.* 2015; **221**: 205–213.

7 Aboulkhair, N.T., Maskery, I., Tuck, C., Ashcroft, I., Everitt, N.M. Improving the fatigue behaviour of a selectively laser melted aluminium alloy: Influence of heat treatment and surface quality. *Mater. Design*. 2016; **104**: 174–182.

8 Fiocchi, J., Tuissi, A., Bassani, P., Biffi, C.A. Low temperature annealing dedicated to AlSi10Mg selective laser melting products. *J. Alloy Compd.* 2017*;* **695**: 3402–3409.

9 Kempen, K., Thijs, L., Van Humbeeck, J., Kruth, J.-P. Processing AlSi10Mg by selective laser melting: parameter optimisation and material characterisation, *Mater. Sci. Tech. Ser.* 2015; **31:8**: 917-923.

10 Beretta, S., Romano, S. A comparison of fatigue strength sensitivity to defects for materials manufactured by AM or traditional processes. *Int. J. Fatigue.* 2017 *;* **94** : 178-191.

11 Wycisk, E., Siddique, S., Herzog, D., Walther, F., Emmelmann, C. Fatigue Performance of Laser Additive Manufactured Ti–6Al–4V in Very High Cycle Fatigue Regime up to $10^9$ Cycles. *Frontiers in Materials*. 2015; **2 (72):** 1-8. doi.org/10.3389/fmats.2015.00072.

12 Siddique, S.,Imran, M., Walther, F. Very high cycle fatigue and fatigue crack propagation behavior of selective laser melted AlSi12 alloy. *Int. J. Fatigue 2017*; **94**: 246-254.

13 Huang, J., Spowart, J.E., Jones, J.W. Fatigue behaviour of $SiC_p$-reinforced aluminium composites in the very high cycle regime using ultrasonic fatigue. *Fatigue Fract. Engng. Mater. Struct.* 2006*;* **29**: 507–517.

14 Suh, M.-S., Suh, C.-M., Pyun, Y.-S. Very high cycle fatigue characteristics of a chrome-molybdenum steel treated by ultrasonic nanocrystal surface modification technique. *Fatigue Fract. Engng. Mater. Struct.* 2013*;* **36**: 768–778.

15 Sander, M., Müller, T., Lebahn, J. Influence of mean stress and variable amplitude loading on the fatigue behaviour of a high-strength steel in VHCF regime. *Int. J. Fatigue.* 2014*;* **62**: 10-20.

16 Fitzka, M., Mayer, H., Schuller, R., Stanzl-Tschegg, S.E., Przeorski, T., Krug, P. Variable amplitude loading of spray-formed hypereutectic aluminium silicon alloy DISPAL® S232 in the VHCF regime. *Fatigue Fract. Engng. Mater. Struct.* 2014*;* **37**: 945–957.

17 Schuller, R., Fitzka, M., Irrasch, D., Tran, D., Pennings, B., Mayer, H. VHCF properties of nitrided 18Ni maraging steel thin sheets with different Co and Ti content. *Fract. Engng. Mater. Struct.* 2015*;* **38**: 518–527.

18 Nikitin, A., Palin-Lucc, T., Shanyavskiy A. Crack initiation in VHCF regime on forged titanium alloy under tensile and torsion loading modes. *Int. J. Fatigue*. 2016; **93 (Part 2)**: 318-325.

19 Yong Huang, Z., Wagner, D., Bathias, C., Chaboche, J.L. Cumulative fatigue damage in low cycle fatigue and gigacycle fatigue for low carbon–manganese steel. *Int. J. Fatigue.* 2016*;* **33 (Issue 2)**: 115-121.

20 Paolino, D.S., Rossetto, M., Chiandussi, G., Tridello, A. *Sviluppo di una macchina a ultrasuoni per prove di fatica gigaciclica*. Proceedings of the 41ᵗʰ AIAS Conference (2012), Vicenza, (In Italian).

21 Tridello, A., Paolino, D.S., Chiandussi, G., Rossetto, M. VHCF response of AISI H13 steel: assessment of size effects through Gaussian specimens. *Procedia Eng*. (2015); **109**: 121–127.

22 Tridello, A. VHCF response of Gaussian specimens made of high-strength steels: comparison between unrefined and refined AISI H13. *Fatigue Fract. Engng. Mater. Struct. 2017;* **40** (Issue 10): 1676–1689.

23 Tridello, A., Paolino, D.S., Chiandussi, G. and Rossetto, M. Effect of electroslag remelting on the VHCF response of an AISI H13 steel. *Fract. Engng. Mater. Struct. 2017;* **40** (Issue 11): 1783–1794.

24 Paolino, D.S., Tridello, A., Chiandussi, G., Rossetto, M. On specimen design for size effect evaluation in ultrasonic gigacycle fatigue testing. *Fatigue Fract. Engng. Mater. Struct.* 2014; **37**: 570–579.

25 Murakami, Y. (2002) Metal Fatigue: Effects Of Small Defects And Nonmetallic Inclusions. Elsevier Ltd, Oxford, UK.

26 Furuya, Y. Notable size effects on very high cycle fatigue properties of high strength steel. *Mater. Sci. Eng. A.* 2011*;* **528**: 5234–5240.

27 ISO/ASTM 52921:2013 (2013) Standard terminology for additive manufacturing -- Coordinate systems and test methodologies. International Standard Organization (ISO), Genève.

28 Biffi, C.A., Fiocchi, J., Bassani, P., Paolino, D.S., Tridello, A., Chiandussi, G., Rossetto, M., Tuissi, A. Microstructure and preliminary fatigue analysis on AlSi10Mg samples manufactured by SLM. *Procedia Structural Integrity. 2017;* **7**: *7-57*.

29 ASTM Standard E1876-09 (2009). Standard test method for dynamic Young's modulus, Shear modulus, and Poisson's ratio by impulse excitation of vibration. ASTM Standard, West Conshohocken (PA).

30 EN ISO 6507-1 (2005) Metallic materials - Vickers hardness test - Part 1: Test method, International Standard Organization (ISO), Genève.

31 Tridello, A., Paolino. D.S., Chiandussi, G., Rossetto, M. Comparison between dog-bone and Gaussian specimens for size effect evaluation in gigacycle fatigue. *Frattura e Integrità Strutturale*. 2013; **26**: 49-56.

32 Tridello, A., Paolino. D.S., Chiandussi, G., Rossetto, M. Gaussian Specimens for Gigacycle Fatigue Tests: Evaluation of Temperature Increment. *Key Eng. Mater.* 2015; **625**: 85–88.

33 Tridello, A., Paolino, D.S., Chiandussi, G., Rossetto, M. Gaussian specimens for VHCF tests: Analytical prediction of damping effects, *Int. J. Fatigue*. 2016; **83**: 36-41.

34 Salmi, A., Atzeni, E., Iuliano, L., Galati, M. Experimental analysis of residual stresses on AlSi10Mg parts produced by means of Selective Laser Melting (SLM). *Procedia CIRP* 2017; **62**: 458 – 463.

35   Masuo, H., Tanaka, Y., Morokoshi, S., Yagura, H., Uchida, T., Yamamoto, Y., Murakami, Y. Effects of Defects, Surface Roughness and HIP on Fatigue Strength of Ti-6Al-4V manufactured by Additive Manufacturing. *Procedia Structural Engineering* (2017); **7**: 19-26.

36 Paolino, D. S., Chiandussi, G. and Rossetto,M. A unified statistical model for S–N fatigue curves: probabilistic definition. *Fatigue Fract. Eng. Mater. Struct.* 2013; **36**: 187–201.

37 Paolino, D.S., Tridello, A., Chiandussi, G. and Rossetto, M. S-N curves in the very-high-cycle fatigue regime: statistical modeling based on the hydrogen embrittlement consideration. *Fatigue Fract. Eng. Mater. Struct.* 2016; **39**: 1319-1336.

38 Borbély, A., Mughrabi, H., Eisenmeier, M., Hoppel, H.W. A finite element modelling study of strain localization in the vicinity of near-surface cavities as a cause of subsurface fatigue crack initiation. *Int. J. Fracture* 2002; 115: 227-232.

39 Mower, T.M., Long, M.J. Mechanical behavior of additive manufactured, powder-bed laser-fused materials. *Mater. Sci. Eng. A*. 2016; **651**: 198–213.

40 Uzan, N.E., Shneck, R., Yeheskel, O., Frage, N. Fatigue of AlSi10Mg specimens fabricated by additive manufacturing selective laser melting (AM-SLM). *Mater. Sci. Eng. A.* 2017*;* **704**: 229–237.

41 Stanzl-Tschegg, S.E. Fracture mechanisms and fracture mechanics at ultrasonic frequencies. *Fatigue Fract. Eng. Mater. Struct.* 1999; **22**: 567–579.

42 Tridello, A., Paolino. D.S., Chiandussi, G., Rossetto, M. Ultrasonic VHCF tests on AISI H13 steel with two different inclusion content: assessment of size effects with Gaussian specimens. *Proceedings of the 7th Conference on Very High Cycle Fatigue, VHCF 7 (2017)*, Dresden (Germany).